npj | clean water

www.nature.com/npjcleanwater

ARTICLE OPEN

Check for updates

Water pumping effect over the organic ions defined graphene oxide membrane impulses high flux desalination

Dian Gong[1,2,8], Xing Liu[3,8], Ping Wu[1,2,8], Yue Wang[1,2,8], Bing Guo[4], Sijia Liu[1,5], Huiling Chen[1,2], Yichen Yin[1,2], Guojuan Liu[1,2], Minghao Liu[1,6], Qiyang Miao[1,7], Chengbing Yu[7]✉, Jingrui Fan[1,2], Zhi Li[1,5], Guosheng Shi[3]✉, Yuhan Sun[1,2,5], Yue He[4]✉ and Gaofeng Zeng[1,2]✉

Graphene oxide (GO) membranes have shown great potential in ionic sieving from aqueous solutions. However, it remains challenging for GO membranes to exclude small ions with a large water flux. Herein, organic ions are confined onto the GO interlaminations to form a precisely restricted 2D channel size of 0.71 nm, which presents >99.9% NaCl rejections and high freshwater fluxes via the pervaporation method, both being orders of magnitude higher than that of common GO membranes. Theoretical calculations reveal that, apart from controlling the 2D channel size of GO by strong cation–/anion–π and π–π interactions, the organic ions act as vapor traps to remarkably shorten vapor diffusion distance and then as water pumps to significantly enlarge water permeability. It not only theoretically explains the low permeability over the common GO membranes with large 2D channels, but also experimentally demonstrates fast and complete desalination on the organic ions-GO membrane.

npj Clean Water (2022)5:68 ; https://doi.org/10.1038/s41545-022-00209-7

INTRODUCTION

Graphene oxide (GO) has triggered much research for membrane separations because the featured 2D channels of stacked GO flakes provide promising separation capability for small species[1–6]. Benefiting from the intrinsic hydrophilicity and sub-nano-sized diffusion channel, water molecules can preferentially interact with the membrane and then diffuse over the 2D channels fueled by the interlaminar capillary effect, which has promoted the applications of GO membranes on selective separation of water from various aqueous mixtures[1,7–11]. With narrowing the 2D channel size and/or functionalizing the channel surface, GO membranes were further adept at a selective separation of small gas molecules, such as H_2, CO_2, and C_2H_6, from certain mixtures[4,5,7,8,12]. As the versatility of GO membranes, there are many interests in introducing GO membranes to membrane desalination, which is one of the most important membrane applications to fill the widening gap between clean water demand and available supply of our thirsty world with a highly effective, energy-saving and continuous operational method[13,14]. However, seawater desalination over GO membranes is still challenged by the inferior performance on both ion rejection and/or water permeability[15]. Therefore, it is desirable to improve both the water permeabilities and salt rejections of GO membranes[16–20].

Due to the weak interlamellar π–π and H bond interactions between GO flakes, the unrestrained 2D channels of GO membranes are inevitably swollen in water, leading to weak exclusion for small ions (e.g., Na^+, Cl^-)[21]. Moreover, the enlarged channels in water do not deliver as high water fluxes as expected, possibly owing to the tortuous path and/or the interactions between leaked salts and channels[22–24]. To cater to small ions separation, many attempts at controllable GO reduction, physical confinement, hetero-species intercalation, and covalent linkages have been made to reduce the channel size of GO membranes[7,8,25–27]. Liu et al. narrowed the 2D channel of GO membrane *via* hydriodic vapor reduction and obtained ~80% higher NaCl rejection than that of the common GO membrane[26]. We controlled the 2D channel size of supported GO membranes by using in situ electro-reduction deposition and achieved >99.9% rejection of NaCl[8]. By periodical covalent linking of GO with bi-site molecules, the 2D interspacing could be well defined, leading to restricted 2D structure and enhanced salt rejection[7]. Recently, we also demonstrated a simple but effective method to control the 2D channel size by introducing alkaline earth cations into the GO membrane[28]. As the interactions between cations and GO (i.e., cation–π interaction) are much stronger than π–π or H bond interactions, the swelling effect of GO membranes was significantly suppressed in desalination, resulting in high rejections for small ions[28,29]. However, water fluxes over these modified GO membranes become smaller due to the narrowed 2D channels. Following the size-sieving mechanism, the 2D channel size of the GO membrane in saline water should locate in the range of ~0.29 nm (kinetic diameter of H_2O) and ~0.72 nm (the bigger one of $(H_2O)_nNa^+$- $(H_2O)_mCl^-$ ion-pair, i.e., hydrated Na^+ size) to allow the diffusion of water but exclude the transport of hydrated Na^+[25]. Accordingly, apart from decreasing membrane thickness, to achieve as high flux as possible, the 2D channel ought to be controlled exactly at 0.72 nm. Inspired by the function of the cation–π effect, it is highly promising to further enhance water flux if ions with larger size and functional groups could be intercalated into the GO membrane.

In this work, a fast and complete desalination was obtained over the organic ion-defined GO membrane. The 2D channel size of the GO membrane was precisely restricted to ~0.71 nm, which is

[1]CAS Key Laboratory of Low-carbon Conversion Science and Engineering, Shanghai Advanced Research Institute, Chinese Academy of Sciences, Shanghai 201210, China. [2]School of Chemical Engineering, University of Chinese Academy of Sciences, Beijing 100049, China. [3]Shanghai Applied Radiation Institute and State Key Lab. Advanced Special Steel, Shanghai University, Shanghai 200444, China. [4]Shanghai Ninth People's Hospital, Shanghai Jiao Tong University, Shanghai 200011, China. [5]School of Physical Science and Technology, ShanghaiTech University, Shanghai 201210, China. [6]Department of Chemical and Environmental Engineering, University of Nottingham Ningbo China, Ningbo 315100, China. [7]School of Materials Science and Engineering, Shanghai University, Shanghai 200444, China. [8]These authors contributed equally: Dian Gong, Xing Liu, Ping Wu, Yue Wang. ✉email: ycb101@shu.edu.cn; gsshi@shu.edu.cn; hey1683@sh9hospital.org.cn; zenggf@sari.ac.cn

nearly equal to the dimension of the hydrated Na ion. The quantum calculations reveal that either organic cations or organic anions can contribute to the size control of the 2D channel through strong cation-/anion–π and π–π interactions, suppressing the swelling effect of GO membrane in aqueous solutions. The classical molecular dynamics simulation posts that the confined organic ions act as vapor traps for the vapor condensation at first, as well as water, pumps to slam liquid water to the permeate side.

RESULTS AND DISCUSSION

Structure and chemistry of organic ion-GO membranes

Organic ions with different structures were intercalated into the supported GO membranes by a facile immersion method (Fig. 1a). Various organic cations or anions with different valency properties, e.g., 1-Vinyl-3-ethylimidazole-tetrafluoroborate ([VElm]BF_4), 1-Butyl-3-methylimidazol-chloride ([BuMlm]Cl), 1-Allyl-3-vinylimidazole-chloride ([AVlm]Cl), 1-Benzyl-3-methylimidazole-chloride ([BeMlm]Cl), Tetramethylthionine chloride (methylene blue, MeB), 2, 7- Naphthalene -disulfonicacid, 3-hydroxy-4-[[2-sulfo-4-[(4-sulfophenyl)azo]phenyl]azo]-tetrasodium (Ponceau S, PS), 3, 3′-[(Biphenyl-4,4′-diyl)bisazo] bis (4-amino-1-naphthalenesulfonic acid sodium) (Congo red, CR), Sodium 4-(Dimethylamino) zaobenzene-4′-sulfonate (methyl orange, MO) and Benzene-sulfonic acid, [[4-[bis[4-[(sulfophenyl)amino] phenyl] methylene]-2,5-cycl (methyl blue, MB), were employed to prepare [VElm]-GO, [BuMlm]-GO, [AVlm]-GO, [BeMlm]-GO, MeB-GO, PS-GO, CR-GO, MO-GO, and MB-GO membranes, respectively, to recognize the ion effects on the membrane properties and desalination performance (Supplementary Fig. 1 and Supplementary Table 1).

The brown GO layer covers the inner surface of the supporting ceramic tube continuously, which is unchanged after the intercalation of organic ions (Fig. 1b inset). The scanning electron microscope (SEM) surface view of the MB-GO membrane reveals dense and defect-free coverages of GO with the typical wrinkles (Fig. 1b). The membrane cross-section views show a highly ordered and well-packed 2D lamellar-structured GO layer on the support with a thickness of ~120 nm (Fig. 1c). Compared with GO membrane, the morphology of MB-GO membrane is almost no change, revealing that the ion-intercalation method is harmless to the membrane integrity (Supplementary Fig. 2). Transmission electron microscope (TEM) images of GO, MB-GO and [AVlm]-GO fragments display the well-ordered carbon layers that are tightly stacked in the in-plane direction (Fig. 1d and Supplementary Fig. 3). Moreover, the fast Fourier transform (FFT) of TEM images reveal that the semiquantitative values of ion-GO interspacing are enlarged by the ion-intercalation in compared with that of GO.

Elemental mapping reveals that the feature element N of organic ions is uniformly distributed on the microstructure of MB-GO and [AVlm]-GO fragments (Fig. 1e and Supplementary Fig. 4). This suggests the successful and uniform intercalation of organic ions. The X-ray photoelectron spectroscopy (XPS) analysis suggests the physical interaction between intercalated organic ions and GO without new chemical bond formation (Fig. 1f and Supplementary Fig. 5). The structural regularity of the samples was analysed by Raman spectroscopy (Fig. 1e). The spectra contain a G-band at 1615 cm^{-1}, arising from the first-order scattering of sp^2 carbon atoms in a 2D hexagonal lattice, and a D-band at 1360 cm^{-1}, ascribed to the vibrations of carbon atoms in plane terminations of disordered graphite[30–34]. Compared to the pristine GO, no visible changes in G- and D-band position were observed for the ion-intercalation GO samples. The intensity ratios of the D and G-band (I_D/I_G), which is sensitive to the level of disorder on the basal plane of GO and defects on the carbon backbone, were almost the same for the pristine GO and ion-intercalation GO samples. It indicates that the ion-intercalation is a physical process without new defects generation for GO. For the wettability, the organic ions tend to slightly decrease the hydrophilicity of the membrane surface (Supplementary Fig. 6).

Structurally, the effects of ion-intercalation and the impacts of separation environments (i.e., water and saline water) on the 2D channel size of [AVlm]-GO membrane (Fig. 2a) and MB-GO membrane (Fig. 2b) were investigated by X-ray diffractions (XRD). The corresponding d values and 2D channel sizes of GO, [AVlm]-GO, and MB-GO membranes in different states were shown in Fig. 2c. For the as-prepared GO membrane in the dry state, it posts a typical diffraction peak of GO (001) centered at $2\Theta = 12.58^o$, reflecting a d value of 7.03 Å. For the [AVlm]-GO membrane, the diffraction peak of the dry sample down-shifted to 9.96^o, corresponding to an enlarged d value of 8.87 Å (Fig. 2a). This suggests that [AVlm]Cl ions were intercalated into GO interlaminar and well-fixed after membrane dehydration. However, unlike the substantial expansion of the GO membrane in water ($2\Theta = 6.44^o$, $d = 13.71$ Å), the corresponding d value of the [AVlm]-GO membrane is significantly limited to ~11.04 Å. Cation–π interactions between metal ions (e.g., Na^+, K^+, Li^+, and Mg^{2+}) and graphitic sheets, which are much stronger than π–π interactions and H bond, have been proven to be effective in narrowing the 2D channels of GO membranes while enhancing the mechanical strength, too[28,29]. As expected, the organic cation, $[AVlm]^+$, also exhibits strong cation–π interactions, which contributes to 2D channel size control. Treated by NaCl solution, similarly, the wetted [AVlm]-GO membrane still displays a much smaller d value than that of the wetted GO membrane (11.18 vs. 13.63 Å). In the redried state, the peak of [AVlm]-GO returns to 10.14^o with the d value of 8.72 Å, which is very close to that of the as-prepared dry [AVlm]-GO (i.e., 8.87 Å). This indicates that the fixed $[AVlm]^+$ cations survived well in the dry-wet-dry cycling due to the strong $[AVlm]^+$-GO interaction. In control, the slight expansion of redried GO was ascribed to the intercalation of NaCl, in line with the reported observations[28]. Furthermore, the d value of [AVlm]-GO can be adjusted in a certain range until the intercalated $[AVlm]^+$ ions reach equilibrium (see details in Supplementary Fig. 7).

Interestingly, similar channel size control effects were still observed, when changing the organic cation $[AVlm]^+$ to the anion $[MB]^{2-}$. The XRD patterns post peaks at 7.74^o and 7.80^o for water-treated MB-GO and NaCl solution-treated MB-GO sample, respectively (Fig. 2b). This reveals that the d value of MB-GO was confined at 11.33–11.41 Å in wet states (Fig. 2c). Moreover, the almost unchanged d values of MB-GO in the beginning (8.72 Å) and ending (8.77 Å) of the dry-wet-dry cycling confirms that the anion-GO interactions can also strongly stabilize the intercalated ions under desalination conditions. Thus, either organic cations or organic anions have the same function on channel size control. The obtained d values were translated to the 2D channel size of membranes by deducting the monolayer thickness of well-reduced GO (~4.0 Å)[35]. As shown in Fig. 2c, both [AVlm]-GO and MB-GO deliver 2D channel size near the size of hydrated Na ion (7.22 Å, the dashed line in Fig. 2c), portending idea sieving effect for NaCl and enough spacing for water permeation.

With quantum calculations, the molecular orbital analyses show that the interactions between $[MB]^{2-}$ and GO mainly comes from the strong anion $[MB]^{2-}$-π interactions and π (ring structure of $[MB]^{2-}$)-π (aromatic rings of graphene) interactions (Fig. 2d)[36]. After the optimization, the most stable configuration of $[MB]^{2-}$ is its parallel rather than perpendicular alignment to the GO sheets. As shown in Fig. 2e, the averaged carbon atoms distance between two graphene oxide sheets is calculated as 8.98 ± 0.84 Å for the optimized geometry, which agrees with the experimental distance of the dry MB-GO membrane ($d = 8.72$ Å).

To evaluate the types of organic ions on the structure control of the GO membrane, various organic ions with different valencies were investigated (Fig. 2f). All ions display suppression effects on the channel size expansion in water, suggesting the universality of

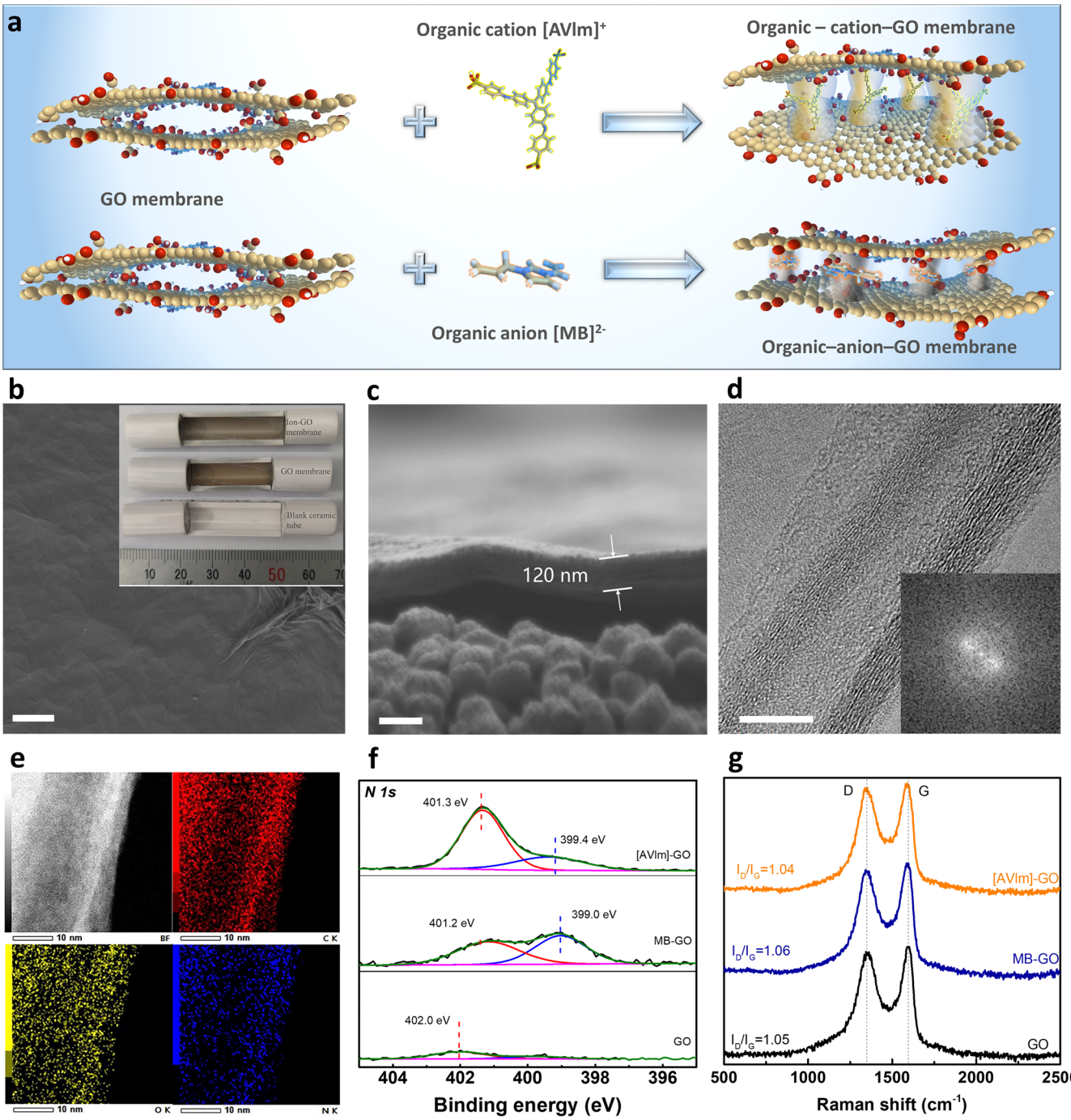

Fig. 1 Organic ions intercalation into GO membranes. a Schematic of organic ion-intercalation between the interlayers of GO flakes by using [AVIm] cations and [MB] anions as examples. SEM (**b**) surface and **c** cross-sectional views of MB-GO membrane (**b** inset: Optical image of the dissected porous ceramic tube and supported GO and MB-GO membranes). **d** TEM image of MB-GO fragment (Inset: the fast Fourier transform of TEM image). **e** Elemental mapping of [AVIm]-GO fragment. **f** XPS N 1 s spectra and **g** Raman spectra of GO, MB-GO, and [AVIm]-GO samples. Scale bars in **b**–**d** are 2 μm, 200 nm, and 20 nm, respectively.

this method. Similar to the [AVIm]-GO and MB-GO membranes, most of the employed organic ions, including $[BeMIm]^+$, $[VEIm]^+$, $[BuMIm]^+$, $[MO]^-$, and $[CR]^{2-}$, can confine the corresponding 2D channel size around 7 Å. However, the negatively charged anion, $[PS]^{4-}$, exhibits a relatively low capacity for channel size control. It is reasonable that the strong charger repels the effect between the highly negative-charged $[PS]^{4-}$ and negative-charged GO (Supplementary Fig. 8) significantly prevents the intercalation of $[PS]^{4-}$. Therefore, the dry PS-GO exhibits small expansion while the wetted PS-GO presents large swelling, due to the low intercalation of PS.

Salt separation on organic ion-GO membranes

The separation performance of organic ion-GO membranes for desalination was investigated by the pervaporation method with NaCl solution (Fig. 3a). The untreated GO membrane yields water fluxes (J_{H2O}) of 1.1 L m^{-2} h^{-1} (LMH) with NaCl rejections (R_{NaCl}) of ~41% at 70 °C, in line with the reported results[26,37,38]. Following

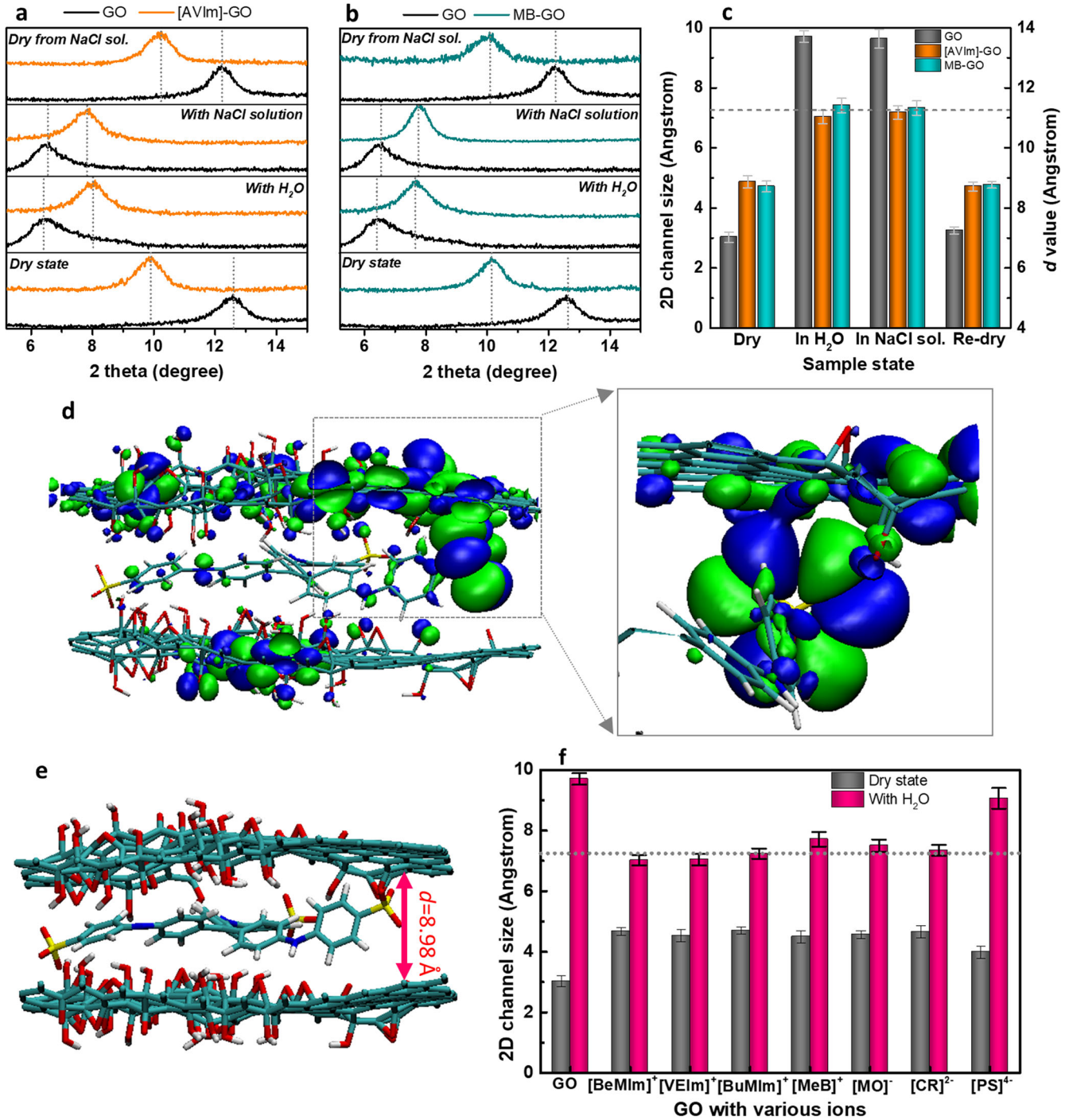

Fig. 2 Ion-intercalation effects on GO membranes. XRD patterns of **a** [AVIm]-GO and **b** MB-GO membranes in dry, wet, NaCl solution-treated and re-dry states. **c** The 2D channel sizes of GO, [AVIm]-GO, and MB-GO membranes in dry, wet, NaCl solution-treated and redried states. The dashed line represents the size of hydrated Na^+ ions i.e., 7.2 Å. **d** The occupied states of the molecular orbitals (HOMO-1) of the MB-GO structure (The electron density is plotted for iso-values of ±0.005 atomic units with green and blue denoting opposite signs) and **e** Side view of optimized MB-GO structure (C, cyan; H, white; O, red; N, blue; P, yellow). **f** The effects of ion type on the control of 2D channel size of GO membranes. The error bars in (**c**) and (**f**) are the standard error of the mean (s.e.m).

treatment with small (earth) alkali metal ions of Na^+ or Mg^{2+}, the ion-GO membranes exhibit nearly complete R_{NaCl} but still, low $J_{H2O} = 0.9–1.7$ LMH because the strong cation–π interactions narrowed the 2D channel size[28]. In contrast, J_{H2O} was significantly improved by one order of magnitude to 15.8–18.9 LMH while R_{NaCl} of 99.5–99.9% was maintained over CR-GO, [VElm]-GO, [BuMIm]-GO, [AVIm]-GO, and MB-GO membranes.

For NaCl removal, the size of hydrated Na^+ (~7.2 Å) is the cut-off point for the size-sieving membrane because the charge neutrality is dominated by the larger ion in the Na^+-Cl^- pair. Taking the thickness of well-reduced GO mono-sheet (~4.0 Å) into account[35], the 2D channel sizes ($D_{channel} = d$ value - 4.0) of CR-GO, [VElm]-GO, [BuMIm]-GO, [AVIm]-GO and MB-GO in the wet state are ~7.1 Å, close to the size of hydrated Na^+, which explains not only the precise sieving effect for hydrated Na^+ but also the maximized

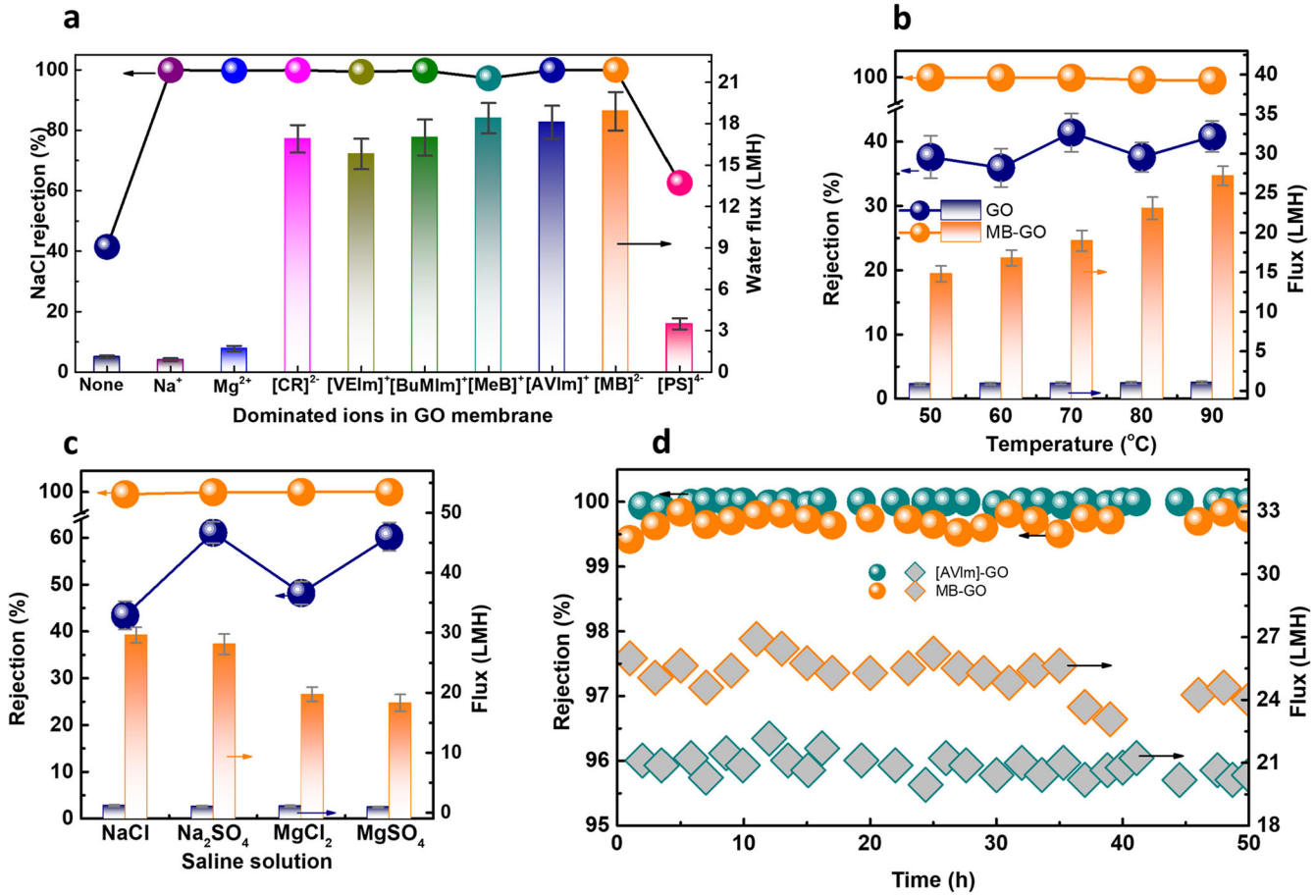

Fig. 3 Desalination behaviors on organic ion-GO membranes. a Effects of cation or anion intercalation on the desalination performance of GO-based membranes (pervaporation conditions: $P = \sim 200$ Pa, $T = 70$ °C, $C_{NaCl} = 3.5$ wt%). **b** Temperature dependence of desalination with GO membrane and MB-GO membrane ($P = \sim 200$ Pa, $C_{NaCl} = 3.5$ wt%). **c** Effects of ionic valence on the desalination with GO and MB-GO membranes ($P = \sim 200$ Pa, $T = 70$ °C, $C_{salt} = 3000$ ppm, the same legends as that in Fig. 2b). **d** Long-term stabilities of MB-GO and [AVIm]-GO membranes for desalination (($P = \sim 200$ Pa, $T = 70$ °C, $C_{NaCl} = 1$ wt%). The error bars in (**a**–**c**) are the standard error of the mean (s.e.m).

space for water transfer. In contrast, the enlarged $D_{channel} = 9.7$ Å of untreated GO membrane fails to exclude hydrated Na^+, in line with its inferior performance of NaCl rejections in real separation. Similarly, the MeB-GO membrane displays a little bit lower R_{NaCl} of 97.2%, which is ascribed to its slightly large $D_{channel} = 7.7$ Å. Moreover, PS-GO shows both low R_{NaCl} of ~62.6% and J_{H2O} of ~3.5 LMH because the highly negatively charged $[PS]^{4-}$ anions are difficult to intercalate into the negatively charged GO membrane.

The flexibility of organic ion-GO membranes on various desalination conditions was further tested. R_{NaCl} of the MB-GO membrane stays high (>99.5%) and stable between 50–90 °C and the corresponding J_{H2O} increases rapidly from 14.8 LMH at 50 °C to 27.2 LMH at 90 °C, which are orders of magnitude higher than those of untreated GO membrane ($R_{NaCl} = 35.9$–41.6% and $J_{H2O} = 0.8$–1.1 LMH) under the same conditions (Fig. 3b). By changing the NaCl concentration from 0 to 3.5 wt%, the MB-GO membrane keeps nearly complete R_{NaCl} with J_{H2O} gradually decreasing from 39.5 LMH for pure water feeding to 29.6 LMH (0.3 wt% NaCl feeding) and further to 19.0 LMH (feeding of 3.5 wt% NaCl solution) at 70 °C (Supplementary Fig. 9).

The effects of divalent ions SO_4^{2-} and Mg^{2+} on the separation were tested by using the diluted salt solutions, as shown in Fig. 3c. The MB-GO membrane demonstrates high salt rejections with large J_{H2O} of 29.6 LMH (NaCl), 28.1 LMH (Na_2SO_4), 19.7 LMH ($MgCl_2$), and 18.3 LMH ($MgSO_4$). In contrast, the untreated GO membrane has significantly lower salt rejections (41–61%) because the hydrated ion sizes, 6.6 (Cl^-), 7.2 (Na^+), 7.6 (SO_4^{2-}), and 8.6 Å (Mg^{2+})[35,39], are all smaller than the $D_{channel}$ of GO membranes in water. Instead, the non-sieving mechanism of the Donnan exclusion mechanism contributed to the salt rejection of the GO membrane due to its negatively charged surface (Supplementary Fig. 8)[40].

Compared with common inorganic membranes that have high NaCl rejections, the MB-GO membrane is superior in ion exclusion and/or water permeability to that of common/2D channel-controlled GO membranes, the multiwall carbon nanotube membranes, the zeolite/MOFs and ceramic membranes (Supplementary Fig. 10 and Supplementary Table 2)[41–43]. As the ion-π interactions endow the membrane with mechanical and structural strength, the MB-GO and [AVIm]-GO membranes maintained stable R_{NaCl} (>99.5%) with high J_{H2O} (20.8 ± 0.8 and 24.9 ± 1.2 LMH, respectively) at 70 °C with 1 wt% NaCl feeding solution during 50 h tests (Fig. 3d).

Pumping effect of organic ions for water transfer

To understand the extraordinary water flux over organic ion-GO membranes, classical molecular dynamics simulations were performed by using the MB-GO system as an example. According to the experimental XRD results, the *d* value 13.6 Å of GO membrane and the *d* value 11.4 Å of MB-GO membrane in NaCl solution were used for the simulations. Considering that GO consists of mainly hydrophobic areas of aromatic rings with few hydrophilic oxygen-containing groups[44–47], we built and simulated a hydrophobic model to investigate the vapor transfer

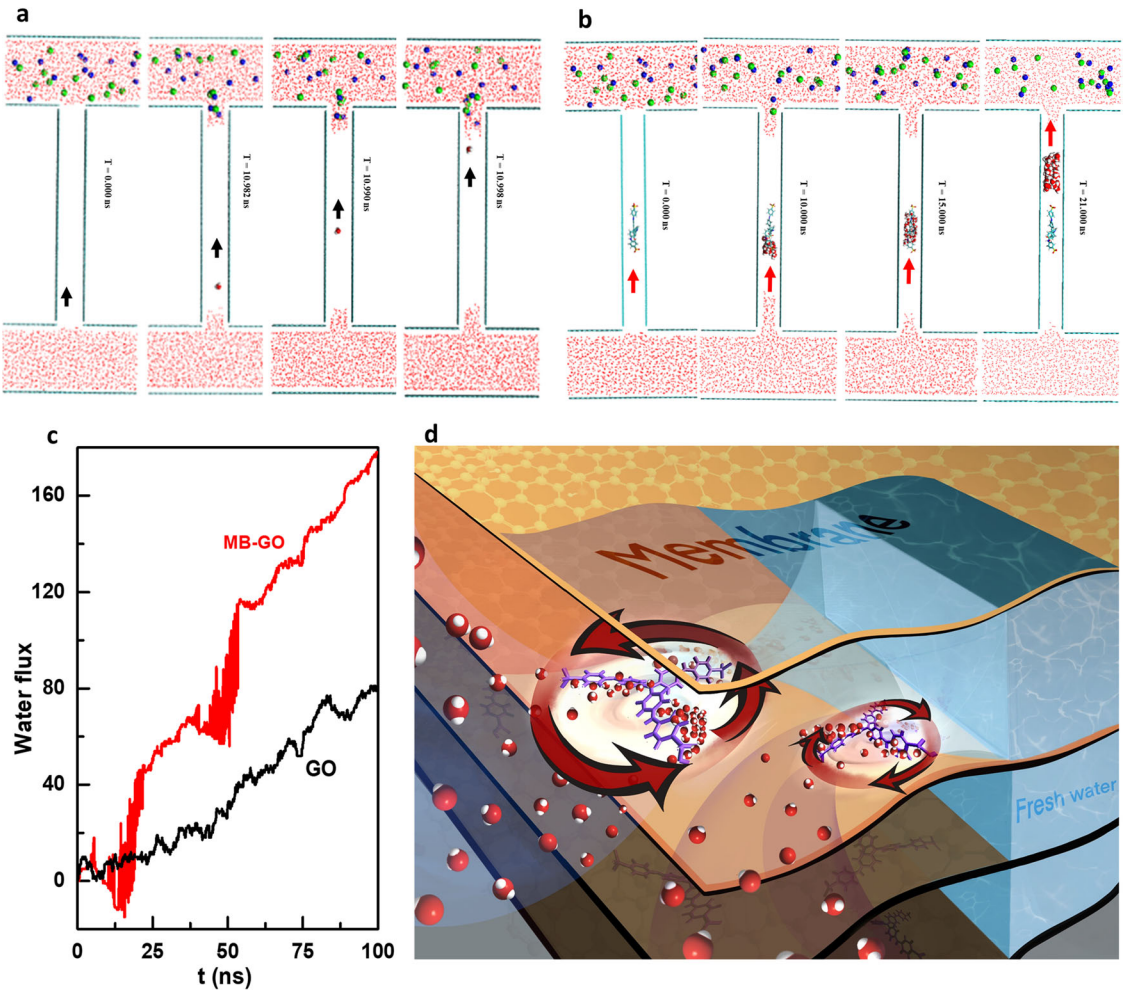

Fig. 4 Molecular dynamics simulation of water permeation through GO-based membranes. Molecular dynamics (MD) simulation snapshots of water (vapor) diffusion through **a** GO 2D channel ($d = 13.6$ Å) at 0 to 10.998 ns and **b** MB-GO 2D channel ($d = 11.4$ Å) at 0 to 21 ns. Na, blue; Cl, green; C, cyan; H, white; O, red; P, yellow. **c** Water fluxes in MB-GO and GO systems. The simulation system consists of 0.4 mol L^{-1} NaCl solution on one and pure water on the other side of two 10 nm long layers of graphene. The MB molecule was put in the middle of the graphene channel according to the quantum calculation for geometries. It generates a chemical potential gradient across the gap, which drives vapor transport from the pure water side to the salt solution side. The net water flux across the middle cross-section is measured. **d** Schematic of the pumping process on organic ions for water transfers.

behaviors, firstly[15]. For the GO system, one vapor water molecule migrates directly through the 2D channel via Knudsen diffusion[15,48], which takes 10.998 ns to cover the whole distance (Fig. 4a). In the MB-GO channel, interestingly, the water molecules in the term of vapor firstly reach the intercalated MB anion, followed by aggregating and condensing on MB. Driven by the concentration difference, the aggregated water then leaves MB as a liquid cluster to the permeate side after 21 ns (Fig. 4b). Evidently, the water amount transported through the MB-GO system is sharply increased in compared to the GO system due to the water cluster containing much more water molecules, leading to significantly higher water flux over MB-GO than GO (Fig. 4c).

MB ions play critical roles in the high performance of ion exclusion and water permeability. On one way, the well-controlled 2D channel size defined by MB ions contributes to the high rejection of NaCl due to the dimension exclusion effect. On the other hand, MB ions act as water traps for the vapor condensation at first and as water pumps to push liquid water to the permeate side (Fig. 4d). It has been confirmed that the nanopore aspect ratio and the condensation coefficient (i.e., the probability of vapor molecule condensation) are the key determinants of flux in hydrophobic pores[48–51]. As suggested by the simulation results, the existence of MB remarkably shortens the path distance of vapor, being equal to a decrease in the nanopore aspect ratio, which contributes to the high flux. Moreover, the vapor-attracting effect of MB greatly enhances the condensation probability of vapor, further promoting water flux. Without these effects, therefore, the water flux is relatively low in the case of the GO system, which is consistent with the real experimental results of the GO membrane.

As a GO sheet also contains a hydrophilic area with oxygen-containing groups on the plane edge, a hydrophilic model was built and investigated (Supplementary Fig. 11). In the simulations of the hydrophilic channel, water transports in the term of liquid[51]. MB-GO exhibits complete rejection for NaCl and relatively low water flux due to the confined channel size, while the GO channel allows high liquid water permeability together with leakage of NaCl owing to the swollen channel. As the real experimental flux over the GO membrane is always low, however, it is reasonable that the hydrophilic area of the membrane plays a non-dominant role in water transfer.

In summary, we have previously controlled the 2D channel size of GO at the cutting-off point of hydrated Na ions. We demonstrated that the strong noncovalent organic anion-p

interaction has the same effect as the cation–π interaction on the adjustment of channel strength and size experimentally and computationally. The organic ion-GO membranes feature nearly perfect rejections of the small ions present in seawater, and enable at least one order of magnitude higher water fluxes than those of GO membranes, and reliable stability during pervaporation. MD simulations reveal that the intercalated organic ions act not only as vapor nucleation sites, which decrease the nanochannel aspect ratio and increase the condensation coefficient, but also as water pumps that transfer water in the term of liquid rapidly. The complete salt rejection is ascribed to the strict size-sieving effect. Our findings not only demonstrate fast and complete desalination over modified GO membranes but also offer an adaptive method to control the structure of GO membranes for potential applications.

METHODS

Membrane preparation

Asymmetric porous alumina tubes supplied by Inopor Co. (Germany) were used as support, which are 65 mm long with inner/outer diameter of 7/10 mm and nominal pore size of ~100 nm on the inner surface. Both ends of the tube were glazed, leaving a ~30 mm middle section corresponding to a 6.5 cm^2 surface area for membrane deposition[7,23,52]. GO powder was supplied by Xianfeng Co. (China). The precursor GO membranes were prepared by the pressure filtration method. Typically, 0.6 mL GO suspension (1 mg mL^{-1}) was dispersed in 200 mL pure water by an ultrasonic disperser. Then the diluted GO suspension was driven into the lumen side of the alumina tube by nitrogen in the pressure range of 1 to 8 bar[7]. The as-prepared GO membrane was dried in an ambient atmosphere for 2 h. For the ion-intercalation, the as-prepared GO membrane, which was firstly wrapped by Teflon tape on the outer surface of the alumina tube, was immersed in organic salt solution (0.1 mol L^{-1}) at room temperature for 1 h. The recovered GO membrane was then rinsed with pure water before drying at 40 °C in a vacuum. To investigate the concentration effect of 1-allyl-3-vinylimidazole-chloride ([AVIm]Cl) on the membrane structure, 0.01–0.5 mol L^{-1} [AVIm]Cl solutions were employed.

Membrane separation

The desalination performance of membranes was measured by contact mode pervaporation at 50–90 °C (Supplementary Fig. 12). The membrane was fixed into the module with two ends sealed by O-rings. The saline solution was introduced into the lumen side of the module with a flow rate of 10 mL min^{-1} by a constant pump[23,52]. The permeation side of the membrane module was connected in sequence with a sample collector, which is immersed in a liquid nitrogen cold trap, and a vacuum pump, by which the pressure of the retentate side was kept at ~200 Pa. The collection interval is in the range of 1 to 2 h. The membrane flux was calculated from the weight difference of the sample collector. The sodium salt concentration of the collected sample was determined by a conductivity meter (MP523–03, Sanxin) and confirmed by inductively coupled plasma atomic emission spectrometry (ICP-AES, PerkinElmer Optima 8000). The concentration of magnesium salts was measured by ICP-AES. The water flux (J) and salt rejection ratio (R) were calculated by the following Eqs. (1) and (2).

$$J = \frac{V}{A \times t} \tag{1}$$

$$R = \frac{C_0 - C_i}{C_0} \times 100\% \tag{2}$$

Where V is the volume of permeated liquid (L), A is the membrane surface area (m^2), t is the separation time (h), and C_0 and C_i are the salt concentration (mol L^{-1}) in the feeding side and permeate side, respectively.

Characterization

The morphology and structure of membranes were characterized by scanning electron microscope (SEM, Zeiss SUPRA 55 SAPPHIRE), transmission electron microscope (TEM, JEM-2100), and X-ray diffractometer (XRD, Rigaku Ultima IV). The surface chemistry of the membranes was analysed by X-ray photoelectron spectroscopy (XPS, Thermo Fisher, K-Alpha), energy dispersive spectrometer (EDS) attached to TEM (Oxford Instrument and JED-2300) and FTIR (Nicolet 6700). The carbon state was determined by Raman spectroscopy (Chameleon He-Ne laser generator with $\lambda = 531.6$ nm). The water contact angle was measured by a contact angle tester (OCA20, Dataphysics). The Zeta potential of GO materials were determined by an electrokinetic analyser (Malvern ZS90, UK).

DFT calculation

The system contains methyl blue (MB) molecules between two graphene oxide sheets in a periodic box with dimensions of $x = 27.05$ Å, $y = 21.30$ Å, and $z = 40.00$ nm. The initial distance between two graphene oxide sheets is 9.45 Å. The period boundary conditions are applied to all three dimensions in the computation, and all atoms were free. The geometry optimizations were performed by the BFGS method at PBE/DZVP level. The convergence criteria for the maximum geometry change between the current and the last optimizer iteration and for the maximum force component of the current configuration were 0.005 Bohr and 0.005 Hartree/Bohr, respectively. These computations were carried out with the software CP2K/2.6.1[36].

Classical molecular dynamics simulations

The simulation model referred to in the previous study was built to research water passing through the hydrophobic channel as vapor. The MD simulation was performed for an NVT ensemble with periodic boundaries in all three dimensions using a time step of 1 fs with Gromacs5.0.36 The temperature was controlled by a velocity-rescale thermostat at 323 K. The gromos53a6 force field was used for both the GO/MB-GO and sodium/chloride ion, and the SPC water model is used for water, since it performs best in predicting the saturated vapor pressure near room temperature. The parameter of GO was referred to as previous research[44,45]. The heavy atoms of the MB molecule were constrained by the harmonic potential to keep the MB molecule in the channel during the simulation to mimic the experimental results. The particle mesh Ewald (PME) scheme was used to treat the long-range electrostatic interaction with a cut-off set at 1.2 nm and the same cut-off was used for the van der Waals interactions. The total simulation time was 100 ns. Each system was independently calculated at least three times to obtain statistically reasonable results.

DATA AVAILABILITY

The data that support the findings of this study are available from the authors on reasonable request.

CODE AVAILABILITY

The computation codes that support the findings of this study are available from the authors on reasonable request.

Received: 12 April 2022; Accepted: 15 December 2022;
Published online: 28 December 2022

REFERENCES

1. Wang, S. et al. Two-dimensional nanochannel membranes for molecular and ionic separations. *Chem. Soc. Rev.* **49**, 1071–1089 (2020).
2. Kim, H. W. et al. Selective gas transport through few-layered graphene and graphene oxide membranes. *Science* **342**, 91–95 (2013).
3. Li, H. et al. Ultrathin, molecular-sieving graphene oxide membranes for selective hydrogen separation. *Science* **342**, 95–98 (2013).
4. Shen, J. et al. Membranes with fast and selective gas-transport channels of laminar graphene oxide for efficient CO2 capture. *Angew. Chem. Int. Ed.* **54**, 578–582 (2015).
5. Dou, H. et al. Bioinspired graphene oxide membranes with dual transport mechanisms for precise molecular separation. *Adv. Funct. Mater.* **29**, 1905229 (2019).
6. Liu, G., Jin, W. & Xu, N. Two-dimensional-material membranes: a new family of high-performance separation membranes. *Angew. Chem. Int. Ed.* **55**, 13384–13397 (2016).
7. Yang, J. et al. Self-assembly of thiourea-crosslinked graphene oxide framework membranes toward separation of small molecules. *Adv. Mater.* **30**, e1705775 (2018).
8. Qi, B. et al. Strict molecular sieving over electrodeposited 2D-interspacing-narrowed graphene oxide membranes. *Nat. Commun.* **8**, 825 (2017).
9. Guan, K., Liu, G., Matsuyama, H. & Jin, W. Graphene-based membranes for pervaporation processes. *Chin. J. Chem. Eng.* **28**, 1755–1766 (2020).
10. Wang, Y. et al. Graphene-directed supramolecular assembly of multifunctional polymer hydrogel membranes. *Adv. Funct. Mater.* **25**, 126–133 (2015).
11. Zhang, M., Sun, J., Mao, Y., Liu, G. & Jin, W. Effect of substrate on formation and nanofiltration performance of graphene oxide membranes. *J. Membr. Sci.* **574**, 196–204 (2019).
12. Wang, S. et al. A highly permeable graphene oxide membrane with fast and selective transport nanochannels for efficient carbon capture. *Energ. Environ. Sci.* **9**, 3107–3112 (2016).
13. Ang, E. Y. M. et al. A review on low dimensional carbon desalination and gas separation membrane designs. *J. Membr. Sci.* **598**, 117785 (2020).
14. Sholl, D. S. & Lively, R. P. Seven chemical separations to change the world. *Nature* **532**, 435–437 (2016).
15. Chen, W. et al. High-flux water desalination with interfacial salt sieving effect in nanoporous carbon composite membranes. *Nat. Nanotechnol.* **13**, 345–350 (2018).
16. Xie, A. et al. Graphene oxide/Fe(III)-based metal-organic framework membrane for enhanced water purification based on synergistic separation and photo-Fenton processes. *Appl. Catal. B Environ.* **264**, 118548 (2020).
17. Yang, Y. et al. Large-area graphene-nanomesh/carbon-nanotube hybrid membranes for ionic and molecular nanofiltration. *Science* **364**, 1057–1062 (2019).
18. Zhou, K. G. et al. Electrically controlled water permeation through graphene oxide membranes. *Nature* **559**, 236–240 (2018).
19. Seo, D. H. et al. Anti-fouling graphene-based membranes for effective water desalination. *Nat. Commun.* **9**, 683 (2018).
20. Li, L., Hou, J. & Chen, V. Pinning down the water transport mechanism in graphene oxide pervaporation desalination membranes. *Ind. Eng. Chem. Res.* **58**, 4231–4239 (2019).
21. Nair, R. R., Wu, H. A., Jayaram, P. N., Grigorieva, I. V. & Geim, A. K. Unimpeded permeation of water through helium-leak-tight graphene-based membranes. *Science* **335**, 442–444 (2012).
22. Yeh, C. N., Raidongia, K., Shao, J., Yang, Q. H. & Huang, J. On the origin of the stability of graphene oxide membranes in water. *Nat. Chem.* **7**, 166–170 (2014).
23. Gong, D. et al. Interfacial ions sieving for ultrafast and complete desalination through 2D nanochannel defined graphene composite membranes. *ACS Nano* **15**, 9871–9881 (2021).
24. Mi, B. Materials science. graphene oxide membranes for ionic and molecular sieving. *Science* **343**, 740–742 (2014).
25. Abraham, J. et al. Tunable sieving of ions using graphene oxide membranes. *Nat. Nanotechnol.* **12**, 546–550 (2017).
26. Liu, H., Wang, H. & Zhang, X. Facile fabrication of freestanding ultrathin reduced graphene oxide membranes for water purification. *Adv. Mater.* **27**, 249–254 (2015).
27. Wang, Y. et al. Enhanced water flux through graphitic carbon nitride nanosheets membrane by incorporating polyacrylic acid. *Aiche J.* **64**, 2181–2188 (2018).
28. Chen, L. et al. Ion sieving in graphene oxide membranes via cationic control of interlayer spacing. *Nature* **550**, 380–383 (2017).
29. Shi, G. et al. Ion enrichment on the hydrophobic carbon-based surface in aqueous salt solutions due to cation-pi interactions. *Sci. Rep.* **3**, 3436 (2013).
30. Marimuthu, M. et al. Sodium functionalized graphene oxide coated titanium plates for improved corrosion resistance and cell viability. *Appl. Surf. Sci.* **293**, 124–131 (2014).
31. Yin, Y. C. et al. Ultrafast solid-phase synthesis of 2D pyrene-alkadiyne frameworks towards efficient capture of radioactive iodine. *Chem. Eng. J.* **441**, 135996 (2022).
32. Miao, Q. et al. Constructing synergistic Zn-N4 and Fe-N4O dual-sites from the COF@MOF derived hollow carbon for oxygen reduction reaction. *Small Struct.* **3**, 2100225 (2022).
33. Miao, Q. et al. CoN2O2 sites in carbon nanosheets by template-pyrolysis of COFs for CO2RR. *Chem. Eng. J.* **450**, 138427 (2022).
34. Liu, M. et al. Atomic Co–N4 and Co nanoparticles confined in COF@ZIF-67 derived core–shell carbon frameworks: bifunctional non-precious metal catalysts toward the ORR and HER. *J. Mater. Chem. A* **10**, 228–233 (2022).
35. Joshi, R. K. et al. Precise and ultrafast molecular sieving through graphene oxide membranes. *Science* **343**, 752–754 (2014).
36. Kühne, T. D. et al. CP2K: An electronic structure and molecular dynamics software package - Quickstep: efficient and accurate electronic structure calculations. *J. Chem. Phys.* **152**, 194103 (2020).
37. Han, Y., Xu, Z. & Gao, C. Ultrathin graphene nanofiltration membrane for water purification. *Adv. Funct. Mater.* **23**, 3693–3700 (2013).
38. Han, Y., Jiang, Y. & Gao, C. High-flux graphene oxide nanofiltration membrane intercalated by carbon nanotubes. *ACS Appl. Mater. Inter.* **7**, 8147–8155 (2015).
39. Tansel, B. et al. Significance of hydrated radius and hydration shells on ionic permeability during nanofiltration in dead end and cross flow modes. *Sep. Purif. Technol.* **51**, 40–47 (2006).
40. Zhu, Z. et al. Ultrahigh adsorption capacity of anionic dyes with sharp selectivity through the cationic charged hybrid nanofibrous membranes. *Chem. Eng. J.* **313**, 957–966 (2017).
41. Goh, P. S. & Ismail, A. F. A review on inorganic membranes for desalination and wastewater treatment. *Desalination* **434**, 60–80 (2018).
42. Singha, N. R. et al. Structures, properties, and performances relationships of polymeric membranes for pervaporative desalination. *Membranes* **9**, 70 (2019).
43. Castro-Munoz, R. Breakthroughs on tailoring pervaporation membranes for water desalination: a review. *Water Res.* **187**, 116428 (2020).
44. Li, H. et al. Graphene oxide facilitates solvent-free synthesis of well-dispersed, faceted zeolite crystals. *Angew. Chem. Int. Ed.* **129**, 14278–14283 (2017).
45. Yang, J., Shi, G., Tu, Y. & Fang, H. High correlation between oxidation loci on graphene oxide. *Angew. Chem. Int. Ed.* **53**, 10190–10194 (2014).
46. Tu, Y. et al. Destructive extraction of phospholipids from *Escherichia coli* membranes by graphene nanosheets. *Nat. Nanotechnol.* **8**, 594–601 (2013).
47. Geng, H. et al. Graphene oxide restricts growth and recrystallization of ice crystals. *Angew. Chem. Int. Ed.* **56**, 997–1001 (2017).
48. Lee, J. & Karnik, R. Desalination of water by vapor-phase transport through hydrophobic nanopores. *J. Appl. Phys.* **108**, 044315 (2010).
49. Humplik, T. et al. Nanostructured materials for water desalination. *Nanotechnology* **22**, 292001 (2011).
50. Lee, J., Laoui, T. & Karnik, R. Nanofluidic transport governed by the liquid/vapour interface. *Nat. Nanotechnol.* **9**, 317–323 (2014).
51. Wang, L. et al. Fundamental transport mechanisms, fabrication and potential applications of nanoporous atomically thin membranes. *Nat. Nanotechnol.* **12**, 509–522 (2017).
52. Zeng, G. et al. Dual-role membrane as NH3 permselective reactor and azeotrope separator in urea alcoholysis. *ACS Cent. Sci.* **5**, 1834–1843 (2019).

ACKNOWLEDGEMENTS

We acknowledge the support from the National Natural Science Foundation of China (21878322, 22075309, and U1932123), the Science and Technology Commission of Shanghai Municipality (19ZR1479200 and 22ZR1470100), and the Shanghai Municipal Human Resource and Social Security Bureau.

AUTHOR CONTRIBUTIONS

The original idea was conceived by G.Z. and G.S. The experimental design and data analysis were performed by G.Z., D.G., P.W., Y.W., C.Y., and H.C. G.S. designed the theoretical computations and illustrated the molecular mechanism. X.L. and G.S. performed the computations. The manuscript was drafted by G.Z., D.G., X.L., and G.S.; all authors have approved the final version of the manuscript. D.G., X.L., P.W., and Y.W. contributed equally to this work.

COMPETING INTERESTS

The authors declare no competing interests.

ADDITIONAL INFORMATION

Supplementary information The online version contains supplementary material available at https://doi.org/10.1038/s41545-022-00209-7.

Correspondence and requests for materials should be addressed to Chengbing Yu, Guosheng Shi, Yue He or Gaofeng Zeng.

Reprints and permission information is available at http://www.nature.com/reprints

Publisher's note Springer Nature remains neutral with regard to jurisdictional claims in published maps and institutional affiliations.